Multiaxial Creep Deformation of Single Crystal Superalloys: Modelling and Validation.

H.C.Basoalto, R.N.Ghosh[1], M.G.Ardakani, B.A.Shollock and M.McLean

Department of Materials
Imperial College of Science, Technology and Medicine
Prince Consort Road, LONDON, SW7 2BP, UK

Abstract

The creep behaviour of the single crystal nickel-base superalloy CMSX-4 has been studied under multiaxial loading, using double Bridgman-notch specimens with <001> and <111> nominal axial orientations, at 850°C and net section stresses of 600 to 850 MPa. The creep lives measured were an order of magnitude greater than those obtained with the same load in uniaxial loading. The disposition of the triaxial stress state with respect to crystallographic orientation varies around the perimeter of the notch. The creep-deformed material has been examined by electron back-scatter diffraction (EBSD) to characterise local changes in crystal orientation resulting from creep strain. It is shown that there is a spatial distribution of crystal rotation across the specimen diameter that is consistent with the activation of $<111>\{1\bar{1}0\}$ and $<001>\{110\}$ slip for <001> and <111> specimens respectively. A model of anisotropic creep, developed at Imperial College over a number of years that assumes viscous slip on such a restricted set of slip systems, has been implemented in a commercial finite element code to simulate the notch-creep behaviour. There is good agreement between the computer simulation and the experimental results.

1 Introduction

The development of single crystal technology for the production of blades for gas turbines has been one of the most important developments in aero-engine technology in the past twenty-five years or so. Single crystal turbine blades are now state-of-the-art in modern aero-engines and are being considered for application in industrial turbines for electricity generation. There is now a good understanding of the creep behaviour of these materials under uniaxial loading. In conventional design procedures elastic stress analysis is used and the creep performance is represented by simple measures, such as rupture life or the time to achieve a specific strain. The evolution of engineering design makes additional demands on the formulation of elevated temperature deformation and fracture behaviour. Here, it is necessary to represent the full shape of the creep curve mathematically and to account for the effects of multiaxial loading through appropriate constitutive laws that can be integrated into advanced numerical design

procedures. Empirical representation of an extensive database accounting for all appropriate combinations of stress (including multiaxiality), temperature and orientation is not practicable. Rather, there is a need to develop approaches to interpolation and extrapolation, both to long times and to more complex loading, from relatively sparse databases dominated by steady, uniaxial loading. This requires a detailed appreciation of the life-limiting deformation and fracture processes.

The design of gas turbines for aerospace and industrial applications must satisfy the increasingly stringent and different demands for performance and efficiency, which have resulted in increasingly complex blade designs and service cycles. Consequently, the blades will experience complex multiaxial states of stress, which will vary during service. Models of anisotropic creep that have been developed to represent uniaxial creep data cannot be automatically extended to account for multiaxial and/or variable loading. It is important to characterise experimentally the effects of multiaxial state of stress both on the creep performance and on the operative deformation mechanisms. This will establish whether or not the constitutive relations for anisotropic creep that have been successful in accounting for deformation in uniaxial loading can be extended to multiaxiality in a straight forward manner. The model can then be incorporated into a finite element routine to simulate the behaviour of a multiaxial test piece or a real component.

This paper presents the results of multiaxial creep tests using Bridgman notch specimens. It is particularly concerned with the characterisation of the changes in crystallography resulting from creep deformation due to the multiaxial stresses and of the implications of these measurements for the active slip systems controlling creep. These measurements are used to validate the extension of the Imperial College crystallographic-slip model of anisotropic creep to account for multiaxial loading.

2 The Creep Model

Continuum damage mechanics (CDM) has proved to be a useful means of describing the high temperature deformation of complex engineering alloys. The Imperial College model has its origins in the work of

---

Ion *et al.* [1], who developed an isotropic continuum damage mechanics model that accounted for the dominant tertiary creep behaviour of a range of engineering alloys by a strain softening mechanism associated with the accumulation of mobile dislocations. In order to describe the anisotropic creep behaviour of single crystal superalloys, deformation was assumed to take place by viscous glide along specific glide systems [2]. The ability of the model to represent an extensive uniaxial database and to predict the creep response under complex uniaxial loading at high temperatures has been demonstrated on a number of single crystal superalloys [3-5]. A principal objective of the present work is to further extend the current model to a multiaxial formulation. The model has been presented in some detail previously; only the main elements are described below.

For nickel-base superalloys it is assumed that two families of slip systems are operative that give rise to the anisotropic creep behaviour of single crystals. These are octahedral and cube systems denoted by the sets $G_1 = \{111\} < 110 >$ and $G_2 = \{001\} < 110 >$, respectively. The activity of each k-slip system is determined by the magnitude of the resolved shear stress and the shear strains, $\gamma^{(k)}$, are determined by solving the evolution equations with appropriate boundary conditions. These equations take the general form,

$$\dot{\gamma}^{(k)} = \dot{\gamma}_0^{(k)}(1 - S^{(k)})(1 + \omega^{(k)})$$
$$\dot{S}^{(k)} = \dot{\gamma}_0^{(k)} H^{(k)}(1 - S^{(k)}/S_{ss}^{(k)})$$
$$\dot{\omega}^{(k)} = \beta^{(k)} \dot{\gamma}^{(k)} \qquad (1)$$

where $S^{(k)}$ and $\omega^{(k)}$ are hardening and strain softening state variables, respectively. The hardening describes the partitioning of stress between the hard γ' particles and the matrix, leading to a description of primary creep (Figure 1). The damage state variable $\omega^{(k)}$ is related to the strain softening effect of an increasing mobile dislocation density, which gives rise to a tertiary response on the strain-time curve.
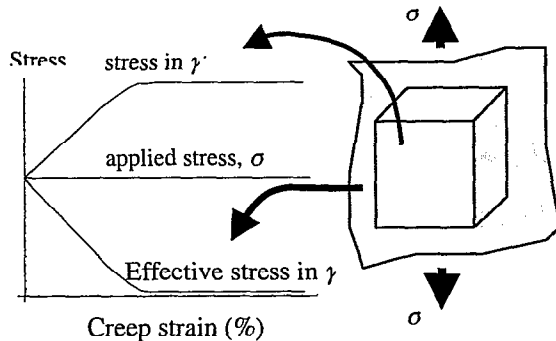

Figure 1

Once the individual $\gamma^{(k)}$'s on all active slip systems have been calculated it is possible determine the macroscopic strain along any direction (e.g. in the direction the tensile load or in any transverse direction). In order to do this we need to determine the deformation rate tensor, $\dot{F}_{ij}$, for an infinitesimal material element. For the k-slip system let the slip plane normal and direction be represented by $n^{(k)}$ and $m^{(k)}$. It can be readily shown that the deformation rate tensor has the following form [6],

$$\dot{F}_{ij} = \sum_{k \in G} \dot{\gamma}^{(k)} m_i^{(k)} n_j^{(k)} \qquad (2)$$

and using $G = G_1 \cup G_2$ then,

$$\dot{F}_{ij} = \sum_{k \in G_1} \dot{\gamma}^{(k)} m_i^{(k)} n_j^{(k)} + \sum_{k \in G_2} \dot{\gamma}^{(k)} m_i^{(k)} n_j^{(k)} \qquad (3)$$

The last result is a simply a statement of superposition, that is, the total deformation rate tensor is the sum of contributions of all active octahedral and cube slip systems. Hence, we can write Equation (3) in a more compact manner,

$$\dot{F}_{ij} = \dot{F}_{ij}^{G_1} + \dot{F}_{ij}^{G_2} + \cdots \qquad (4)$$

The importance of $\dot{F}_{ij}$ is that it describes the deformation of a material element. Thus, once $\dot{F}_{ij}$ is known (determined from the accumulation of shear strains on the active slip systems) then the macroscopic creep response can be obtained. This is achieved by calculating the equivalent strain using a Mises- type relation. In addition to accounting for strain in arbitrary directions, the model predicts local changes in crystal orientation that result from these anisotropic strains.

Isotropic creep models accounting for multiaxial loading in finite element (FE) codes are generally based on an assumption that deformation takes place by shear and, consequently, the von Mises formulation for individual elements can be used. However, in the isotropic case there is no restriction on the choice of slip systems. An isotropic material is assumed to deform on any plane on which the resolved shear stress has the maximum value. This is always equal to half of the effective stress. In terms of crystallographic deformation this means that the Schmid factor is always 0.5. On the other hand, for anisotropic materials the Schmid factor can have any value between 0 and 0.5, depending on the choice of slip system and orientation of the stress axis. The main advantage of this approach is that it allows the use of the uniaxial creep law even for multiaxial loading provided the stress and strains are replaced by an effective stress ($\bar{\sigma}$) and effective strain ($\bar{\varepsilon}$). For example, in power law creep the creep rate is described by the relation $\dot{\varepsilon} = A\sigma^n$, which become $\dot{\bar{\varepsilon}} = A\bar{\sigma}^n$ for multiaxial loading. The expressions for effective stress and effective strain rate ($\dot{\bar{\varepsilon}}$) for isotropic material are as follows,

$$\bar{\sigma}^2 = \frac{1}{2}\left[(\sigma_{11} - \sigma_{22})^2 + (\sigma_{22} - \sigma_{33})^2 + (\sigma_{33} - \sigma_{11})^2\right]$$
$$+ \frac{1}{3}\left[\sigma_{23}^2 + \sigma_{31}^2 + \sigma_{21}^2\right] \qquad (5)$$

$$\bar{\varepsilon}^2 = \frac{\gamma}{2}\left[(\varepsilon_{11} - \varepsilon_{22})^2 + (\varepsilon_{22} - \varepsilon_{33})^2 + (\varepsilon_{33} - \varepsilon_{11})^2\right]$$

$$+ \frac{1}{3}\left[\varepsilon_{23}^2 + \varepsilon_{31}^2 + \varepsilon_{21}^2\right] \qquad (6)$$

For anisotropic material, both of these relations will be functions of the co-ordinate system that defines the state of stress. In the case of a cubic crystal, because of its symmetry the above expressions remain valid if the states of stress and strain are represented with respect to its normal crystallographic axes. Therefore, as long as such a practice is followed, there is no problem in interfacing the slip-based formulation through a user-defined subroutine for the calculation of incremental creep strain at each time-step defined by the commercial finite element code. In the present study the ABAQUS finite element package has been used, where the model was interfaced with the software through a modified creep user-subroutine. This approach is simpler and less computing intensive than incorporating the creep law into ABAQUS through a user-material routine (U-MAT) [7]. Calculations have been carried out for circumferentially notched specimens using the full CDM crystallographic slip model. Previous work has mainly been restricted to Norton-type steady state creep relations [8, 9].

An experimental programme, which has been carried out to begin to evaluate the FE calculations, is the focus of the present work. For this creep tests were carried out using circumferential Bridgman notch specimens in tension, and using electron back-scatter diffraction (EBSD) for characterisation of the deformation under multiaxial stresses [10].

3 Experimental

The experimental programme has been carried out on the commercial single crystal superalloy CMSX4; the chemical composition is given in Table 1. Single crystal castings were supplied by PCC Aerofoil Corporation, using state-of-the-art commercial casting technology. The single crystals were supplied in the fully heat-treated condition. The standard commercial heat treatment (solutioning for 1h/1280°C, 2h/1290°C, 6h/1300°C and ageing for 4h/1140°C, 16h/870°C) produced cuboidal γ' particles with size of about 0.5 μm occupying a volume fraction of about 80%. The initial orientation of each casting was determined by the X-ray Laue back reflection technique; the axial orientation of each cylindrical casting used was within 4° of <001> or <111>.

Double notch Bridgman creep specimens, Figure 2, were machined from the single crystal castings. They were tested at 850°C with net-section stresses in the range 600-850MPa. A shadowgraph technique was used to measure local strain [11]. Fracture surfaces of all test-pieces were examined by optical and scanning electron microscopy. Longitudinal and transverse section of the

uniaxial and multiaxial creep tested samples were electropolished using 10% perchloric and 45% acetic acid in butan-1-ol at 25 V at -5 °C. The EBSD (electron back-scattered diffraction) technique was employed in conjunction with a JEOL 840 scanning electron microscope (SEM) equipped with SINTEF hardware to map the spatial distribution of crystal orientation over these sections. CHANNEL software was used to analyse the three Euler angles φ_1, ϕ, and φ_2 measured by indexing Kikuchi bands. These Euler angles are used by the software for displaying orientation data in the form of inverse pole figure (IPF), pole figure (PF) or orientation map (OM). For details of the procedure see Ref. [10, 12].

Table 1. CMSX4 alloy composition in wt% .

Cr	Co	W	Ta	Al	Ti	Re	Mo	Ni
6	9	6	7	5.6	1	3	0.6	Bal

4. Results

4.1 Creep Rupture life

Figure 3 compares the times to rupture for uniaxial and the multiaxial creep tests of <001> and <111> single crystal of CMSX4 at 850°C. This clearly shows the effect of the multiaxial stress state is to extend the creep life by about an order of magnitude.
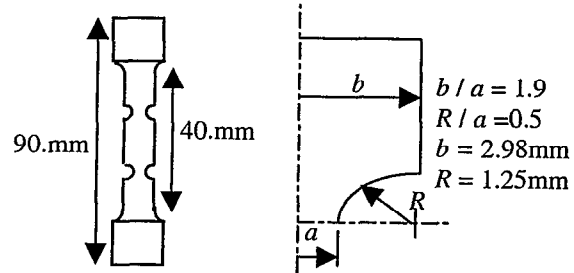

$b/a = 1.9$
$R/a = 0.5$
$b = 2.98$mm
$R = 1.25$mm

90.mm   40.mm

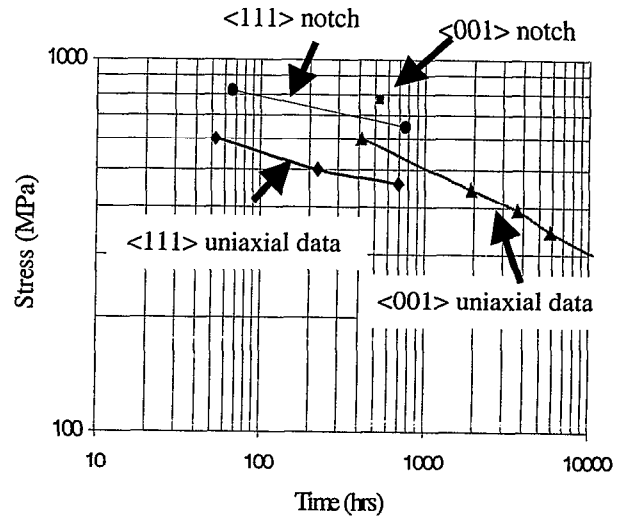**Figure 2** Geometry of double Bridgman notch

Figure 3 Lifetime data for CMSX4 <111> and <001> orientations under uniaxial and multiaxial loading conditions at 850°C.

4.2 Fracture behaviour

The fracture surfaces for the <001> and <111> orientated notch specimens were studied. Figure 4(a) shows the fracture surface for a <001> crystal tested at 775MPa/850°C, clearly showing crystallographic facets with four-fold symmetry consistent with deformation having occurred on the {111} planes that are symmetrically inclined to the load axis. In Figure 4(b) the fracture surface for the <111> orientated crystal shows crystallographic facets with three-fold, cube-on-edge symmetry that is consistent with deformation being constrained by the (001) faces of the γ′ particles.

The fracture surfaces of the multiaxial creep specimens for both <001> and <111> orientated crystals have two quite distinct regions:

- The central zones are jagged and macroscopically perpendicular to the tensile axis,

- There is a smoother outer ring showing less obvious crystallographic character; the width of this

zone decreases with increasing load. Figure 5 shows the fracture surfaces for <111> tests.

4.3 Lattice Rotations

The present authors have used EBSD extensively to measure lattice rotations resulting from creep deformation of uniaxially loaded specimens [11]. Large rotations are found in specimens that deviate significantly from the high symmetry <001> and <111> orientations. In the case of near <001> and <111> there is some spread in orientation as a result of creep strain, but the mean orientation remains unchanged.

Figure 6(a) show the orientation map (OM), Inverse pole figure (IPF) and (111) pole figure obtained from transverse section of as received [001] single crystal. Although the OM exhibits a contrast change across the section, the maximum misorientation measured is ± 0.5°.
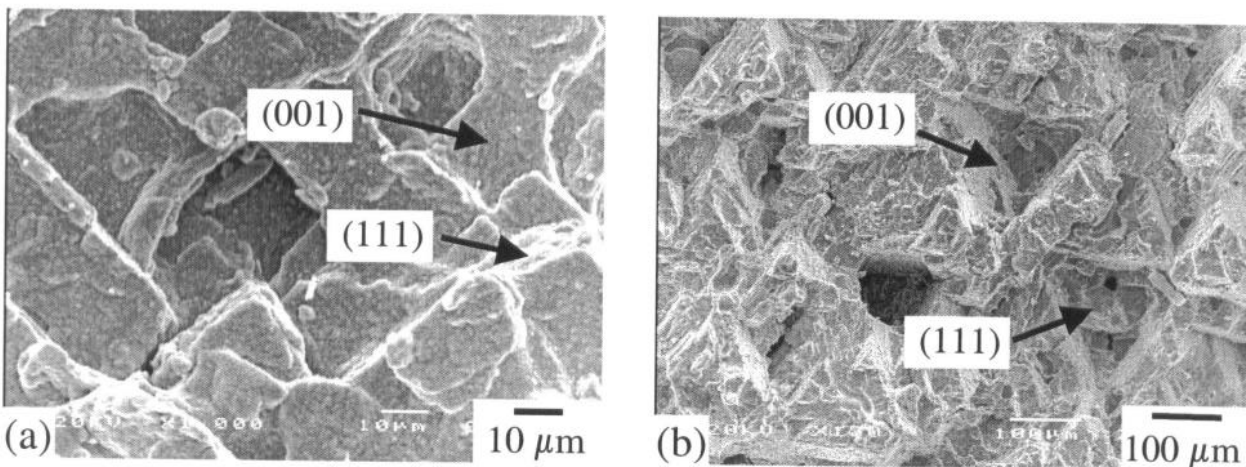
Figure 4 SEM of the fracture surfaces for (a) CMSX4<001> at 775MPa/850°C,
and (b) CMSX4 <111> at 650MPa/850°C.
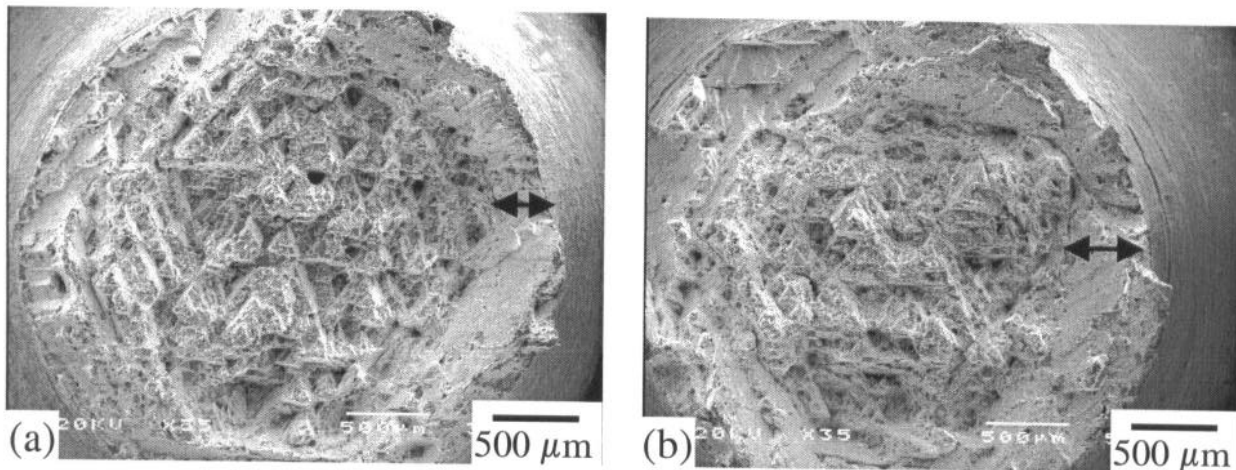
Figure 5 Fracture surfaces of CMSX4 <111> crystals tested at 850°C
(a) 820MPa, and (b) 650MPa.

figure 6(b), (IPF) and (111) pole figure. Figure 7 shows a transverse section of a uniaxially loaded <111> specimen tested to fracture; no systematic trend in crystal rotation is observed. The OM shows a uniform contrast and the maximum misorientation is about ±2°. Thus, in uniaxial tests it is found that the crystal rotation for the stable <001> and <111> single crystals is minimal. As will be shown, this is found to be in marked contrast when looking at the case of multiaxial deformation. Figure 8 shows the range of orientations observed on a longitudinal section of a Bridgman-notch creep specimen tested to fracture at 820MPa/850°C. It shows that the deformation is highly localised and that there are regions where very significant lattice rotations have occurred from Y to Y1 (see Figure 8(d)). In the zone of most intense deformation there is clear evidence of mechanical twinning having occurred.

Transverse sections through the minimum diameter of the notch were prepared by polishing one fracture surface until a flat surface was obtained. This was then electro-polished as described above. Figure 9 shows the results of EBSD analysis of the transverse section of a <001> specimen tested at 755MPa/850°C. In Figure 9(a) orientation map, inverse pole figure (IPF) and (111) pole figure for the entire section are shown. The orientation map clearly shows the four-fold symmetry associated with the <001> axis. The map was generated using a grid of 150×150 with a step size of 20μm, and a beam spot of approximately 1μm. There has been a spread of orientation of $\pm15^0$ from the initial near-<001> orientation of the initial specimen. Further analysis of the data shows that the perimeter of the section at diameters pointing in <110> directions shows a rotation from <001> towards <111> on the IPF (Figure 9(b)). However, at the perimeter of diameters pointing in the transverse cube directions (<100> and <010>) the rotation is from <001> to <101>, see Figure 9(c). The Pole Figures show that the (111) poles rotate in different directions, depending on position on the section perimeter, forming cruciforms.

Similar data for a <111> notch specimen creep tested to fracture at 820MPa/850°C are shown in Figure 10. Here the three-fold symmetry of the <111> axis is clearly apparent in the orientation map. The overall deviation from <111> is $\pm20^0$. However, again the crystal rotations observed vary systematically around the circumference of the section. In transverse radii pointing towards <211> the rotation on the IPF is from <111> to <001> (Figure 10(b)) and for radii pointing to <011> the rotation is from <111> towards <101> (Figure 10(c)). At the centre of the section there is a small spread of orientations, but they are all within $\pm5^0$ of <111> (see Figure 10(d)).

Furthermore, it can be seen from Figures 9 and 10 that the <001> crystal has been divided into approximately 100 subgrains, whereas for the <111> crystal less than

marked difference are currently under investigation.

4.4 Finite Element simulation

The crystallographic slip model, with parameters established by analysis of a uniaxial creep database, has been used to simulate the deformation of Bridgman notch specimens. The FE analysis was carried using the commercial package ABAQUS, and the model was interfaced using a modified creep user-subroutine [7]. An example of the output is shown in Figure 11, which shows a transverse section through the minimum notch diameter for a <001> specimen tested at 400MPa/850°C. The four-fold symmetry is readily apparent. In the example shown there is the accumulation of significant strains at the perimeter of the section (1.5 to 2.5%) but very low strains (0.5%) at the centre.

5 Discussion

The creep rupture data show that there is significant notch-strengthening that is similar to the level observed in polycrystalline superalloys. For isotropic materials the notch is considered to play two roles:

- It locally amplifies the axial component of stress σ_{ZZ} at the notch root giving rise to localised deformation and redistributing load to the specimen centre, and
- The radial component of stress σ_{RR} reduces the resolved shear stress and inhibits deformation.

The observations on the fracture surfaces are quite consistent with deformation being concentrated at the section perimeter. The smooth outer ring is typical of a creep failure. As the load-bearing section is reduced, the stress on the interior of the specimen increases to a level where fast fracture occurs; this is characterised by the jagged crystallographic facets that are observed.

As indicated in Section 2, the normal assumption of shear occurring in the direction of maximum shear stress, which is central to the von Mises formulation, is not valid for single crystals where the influence of specific slip systems is thought to be important. Clearly, the spatial distribution of lattice rotations observed by EBSD and illustrated in Figures 9 and 10 confirm this view.

Assuming elastic isotropy, which should be valid for a cubic system, the initial elastic stress field around the Bridgman notch in polar form is given by the expressions [13]:
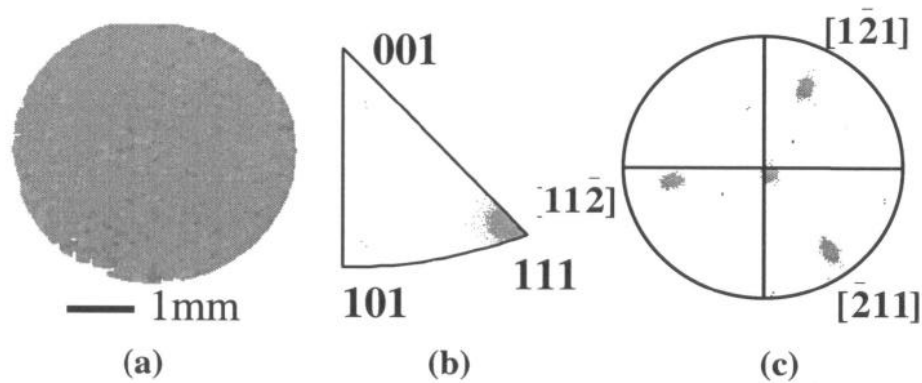
$$\sigma_{zz} = F\left[1 + \log\left(\frac{a^2 + 2aR - r^2}{2aR}\right)\right] \tag{7}$$

$$\sigma_{rr} = F\log\left(\frac{a^2 + 2aR - r^2}{2aR}\right) \tag{8}$$

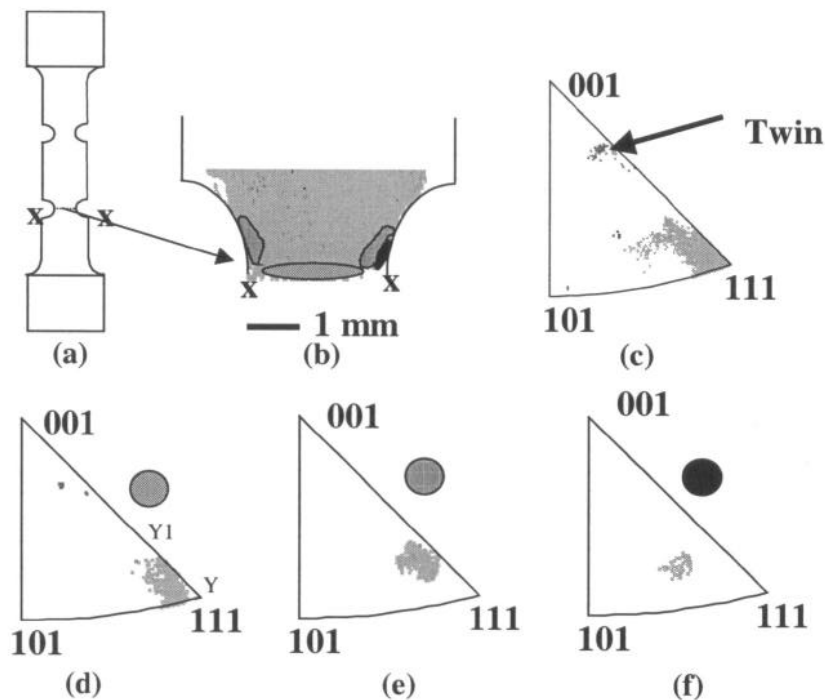$$\sigma_{rr} = \sigma_{\theta\theta} \tag{9}$$
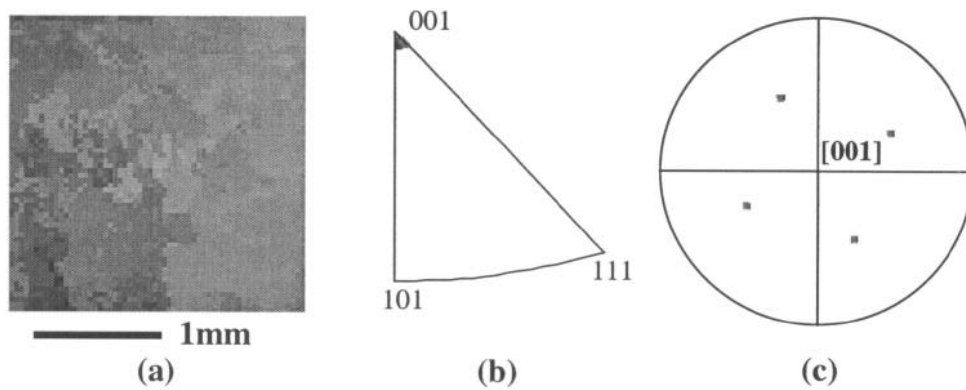
Figure 6 Transverse section of as received [001] single crystal (a) Orientation map, (b) (IPF) and (c) (111) pole figure.

Figure 7 Transverse section, near fracture surface, of uniaxially loaded [111] single crystal creep tested at 850°C/460MPa. (a) orientation map, (b) inverse pole figure (IPF), (c) (111) pole figure.


Figure 8 Longitudinal section of [111] single crystal creep tested at 850°C/820 MPa showing, (a) the position of fractured area (b) orientation map, (c) overall orientations of the map, (d, e and f) orientation of subsets shown in (b).
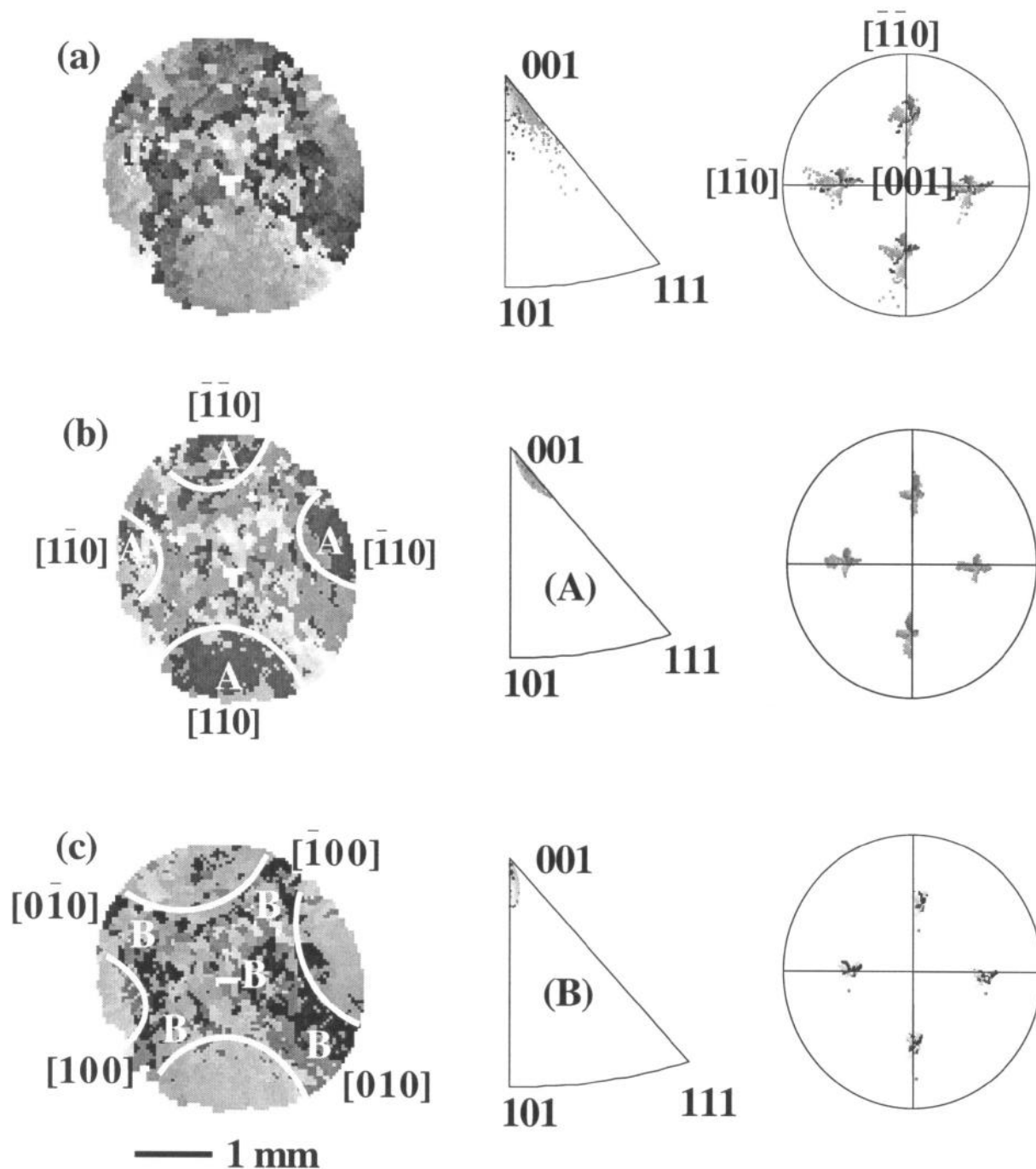
Figure 9 Transverse section, near fracture surface, of notched [001] single crystal tested at 850°C/775 MPa. (a) Overall orientation map, inverse pole figure (IPF) and (111) pole figure. (b) Orientation map showing four-fold symmetry of deformation at (A), IPF and (111) pole figure show the local orientation of subsets marked (A). (c) Orientation map, IPF and (111) pole figure showing the local orientation of subsets marked (B).
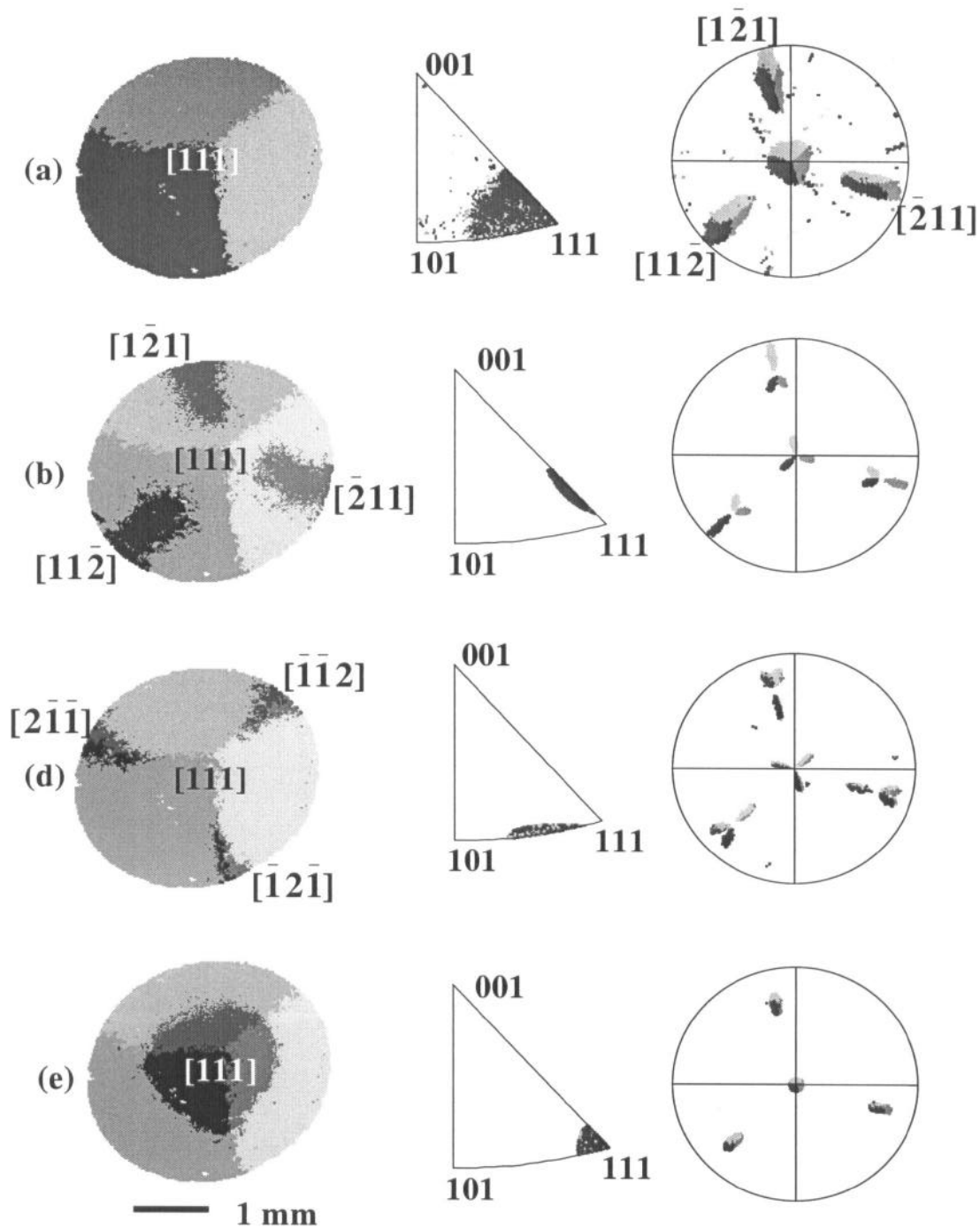
Figure 10 Transverse section, near fracture surface, of notched [111] single crystal tested at 850°C/820 MPa. (a) Overall orientation map, inverse pole figure (IPF) and (111) pole figure. (b, c) Orientation map showing three-fold symmetry of deformation, IPF and (111) pole figure showing the local orientation of (dark contrast). (e) Orientation map, IPF and (111) pole figure showing the local orientation of subsets at the centre.
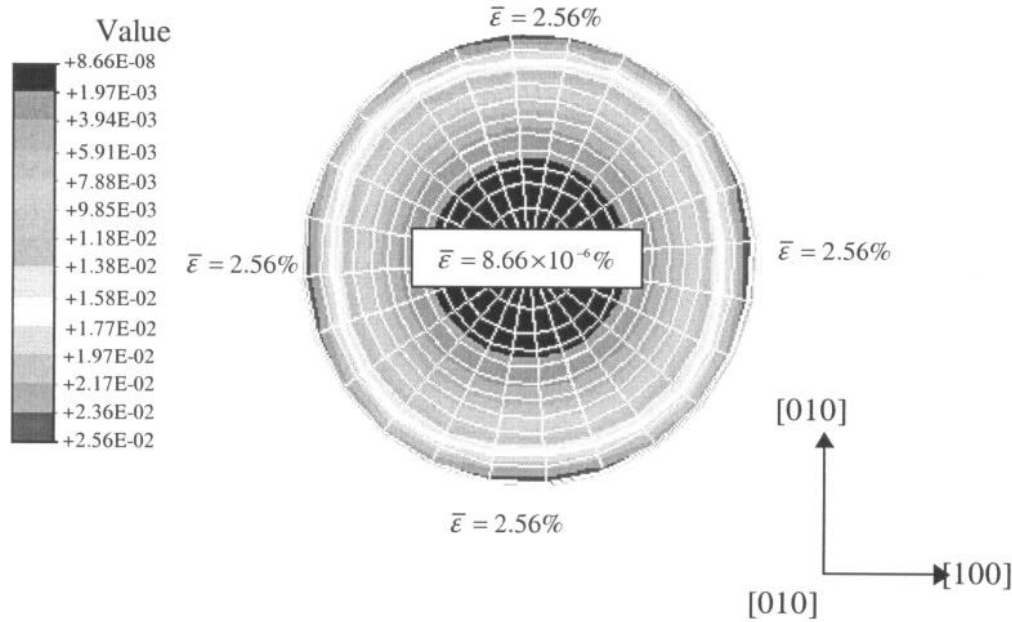
Figure 11 Finite element calculation of the equivalent strain, $\bar{\varepsilon}$, using anisotropic slip model for a <001> orientated crystal at 400MPa/850°C.

where F is the applied load, a the outside radius of the cross section of neck, R radius of curvature at the neck, r position along the cross section.

For exact <001> and <111> orientations the axial σ_{ZZ} component leads to equal and symmetrically distributed resolved shear stresses on the active slip systems so that deformation retains the original orientation. Any deviation from the exact orientation amplifies the shear stress on one or two systems and reduces it on others. This is exactly the situation for uniaxially stressed specimens, except that there is a stress concentration in the case of the notch. The σ_{RR} component which is at right angles to the axial stress has the same general effect as a misorientation in a uniaxial specimen in that it amplifies some resolved shear stresses and reduces others. An important difference is that σ_{RR} amplifies different slip systems in different positions of the specimens.

For <001> specimens the axial load leads to a maximum resolved shear stress for octahedral slip. There has been debate on whether this occurs with <110> or <211> Burgers vector; however, there appears to be a consensus that the latter predominately occurs at low temperatures and high stresses where γ' cutting is possible [14]. The effect of the radial component of stress on the possible slip systems is shown as maximum Schmidt factors in Figure 12. The two octahedral systems have similar values each varying by about 20% with a periodicity of 45^0. The radial

component in the direction <010> will enhance the shear stress on $(1\bar{1}1)(011)$ and lead to a rotation of the specimen axis from <001> towards <011>. On the other hand, the radial component in the direction $\langle\bar{1}10\rangle$ will enhance the shear stresses on both $(1\bar{1}1)(011)$ and $(1\bar{1}1)(\bar{1}01)$ and this will lead to a rotation of <001> towards $\langle\bar{1}11\rangle$. This is exactly the behaviour that is observed.

For <111> specimens, the effect of σ_{RR} is quite different at opposite ends of a diameter of a transverse section. Here the maximum shear stress due to the axial load is on (100)<011> type slip systems. The σ_{RR} at the $\langle11\bar{2}\rangle$ radius enhances the $(001)(110)$ slip vector and consequently leads to a rotation of <111> towards <110>. However, at the opposite end of the diameter, towards $\langle\bar{1}\bar{1}2\rangle$, two cube slip systems are enhanced- (100)<011> and (010)<101>. The combined effect is a rotation of <111> towards <001>. Again, this is quite consistent with the EBSD observations.

This analysis, based on the initial elastic stress field, can only be indicative. In practice, there will be a redistribution of stress as a result of creep deformation at the notch root. It requires a full time-dependent plastic analysis to account for this effect. Nevertheless,

the present measurements of micro-crystallographic changes and the approximate analysis provide strong support for the basic assumptions of the crystallographic slip model, which incorporates both octahedral, and cube slip. This gives confidence in extending the uniaxial model to account for deformation in multiaxial stresses and to implement in FE simulations of specimen or component behaviour.
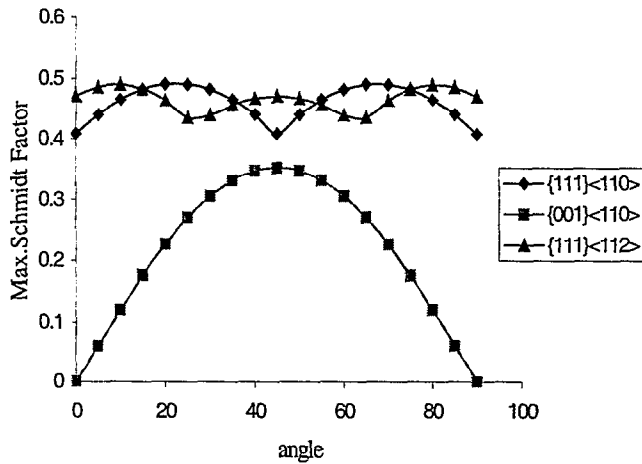
Figure 12 Maximum Schmidt factor due to radial stress component σ_{RR} calculated for [001] direction..

6. Conclusions

1. The multiaxial stress state produced by a circumferential Bridgman notch increases the creep rupture lives of CMSX4 by an order of magnitude relative to the net-section tensile uniaxial stresses in the <001> and <111> directions.

2. Creep deformation of <001> and <111> specimens leads to changes in orientation of up to 20^0 that vary across the specimen section.

3. Crystallographic analysis shows that the observed orientation changes are consistent with the radial component of the multiaxial stress state modifying the resolved shear stress for crystallographic slip such that the $(111)(\bar{1}10)$ and $(001)(110)$ systems operate on <001> and <111> loaded specimens respectively.

4. The results are consistent with the Imperial College model of anisotropic creep which has been implemented in a commercial FE code to simulate the creep behaviour of notch-creep specimens. There agreement between experimental observation and FE simulation is promising.

8. List of References

1. J.C. Ion et al., Report DMA A115, The National Physical Laboratory, Teddington 1986

2. R.N. Ghosh and M. McLean, Acta Metal. Mater., 1990, Vol. 40 , p. 1977

3. R.N. Ghosh, R.V. Curtis, and M. McLean, Acta metall. mater., 1990, Vol. 38, p.1997.

4. L-M.Pan, B.A.Shollock and M.McLean, Proc. R. Soc. Lond. A, 1997, **453**, 1689-1715.

5. H.Basoalto, M. Ardakani, R.N. Ghosh, B.A Shollock and M. McLean,2000, Key Eng. Materials, Vol. 171-174, p.545.

6. D.Peirce, R.J.Asaro, and A.Needleman, Acta metall., 1982, Vol. 30, p. 1087.

7. ABAQUS user's manual, version 5.4.

8. N. Ohno, T. Mizuno, H.Kawaji, and I.Okada, Acta metall. mat., 1992, Vol. 40, p. 567.

9. L.Meric,P.Poubanne, and G.Cailletaud, Trans. ASME, 1991, vol. 113, p.162.

10. D. J. Dingley and V. Randle, J. Mater. Sci. 1992, Vol. 27,p. 4545.

11. M.B.Henderson, L.M.Pan, B.A.Shollock and M.Mclean, Proc. Euromat, 1995, Symp. D, 25/9-28/9, Pdua/Venice,1-10

12. F. J. Humphreys. J. Microscopy, 1999, Vol. 195, p.170.

13. B.P.W. Bridgman, Large Plastic Flow and Fracture, Metallurgical Series, McGraw-Hill Book Company Inc., 1952.

14. B.A. Shollock, M. Ardakani, R.N.Ghosh, H.Basoalto and M.Mclean, 1999, Proc. of Plasticity '99, Neat Press, p.193